Oxygen Vacancy Linear Clustering in a Perovskite Oxide

Kitae Eom,[†] Euiyoung Choi,[†] Minsu Choi,[†] Seungwu Han,[‡] Hua Zhou,[§] and Jaichan Lee*[,†]

[†]School of Advanced Materials Science and Engineering, Sungkyunkwan University, Suwon 16419, Korea
[‡]Department of Materials Science and Engineering, Seoul National University, Seoul 08826, Korea
[§]Advanced Photon Source, Argonne National Laboratory, Argonne, Illinois 60439, United States

Ⓢ Supporting Information

ABSTRACT: Oxygen vacancies have been implicitly assumed isolated ones, and understanding oxide materials possibly containing oxygen vacancies remains elusive within the scheme of the isolated vacancies, although the oxygen vacancies have been playing a decisive role in oxide materials. Here, we report the presence of oxygen vacancy linear clusters and their orientation along a specific crystallographic direction in $SrTiO_3$, a representative of a perovskite oxide. The presence of the linear clusters and associated electron localization was revealed by an electronic structure represented in the increase in the Ti^{2+} valence state or corresponding Ti $3d^2$ electronic configuration along with divacancy cluster model analysis and transport measurement. The orientation of the linear clusters along the [001] direction in perovskite $SrTiO_3$ was verified by further X-ray diffuse scattering analysis. Because $SrTiO_3$ is an archetypical perovskite oxide, the vacancy linear clustering with the specific aligned direction and electron localization can be extended to a wide variety of the perovskite oxides.
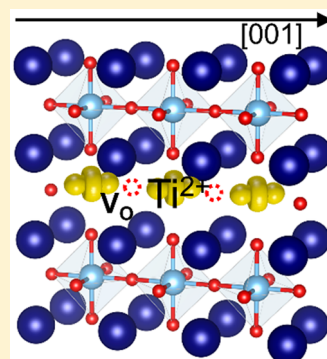
Oxygen vacancy is one of the fundamental and intrinsic defects in oxides and has displayed critical impacts in the evolution of the physical properties. Moreover, oxygen vacancies are easily introduced into the oxides via various processes such as growth and annealing in reducing atmospheres. In general, two electrons are left behind upon creation of an oxygen vacancy. Those electrons are expected to increase with the oxygen deficiency, and the character of the electrons, either extended or localized, primarily determines a very initial direction in further evolution of physical properties where the electrons are coupled with electronic and crystal structures. Thus, a fundamental understanding of oxygen vacancies is critical for further progress toward oxide material understanding and electronic devices.

Perovskite oxides with a simple cubic crystal system constitute an important class of oxides exhibiting a wide variety of electronic and magnetic properties. The high-T_c superconductivity,[1,2] exotic magnetism,[3,4] metal−insulator transition,[5] large dielectric response,[6] and ferroelectricity[7] are prominent examples. Its simple crystal structure leads to many common structural features but various physical properties and thus allows for extensive study. Particularly, $SrTiO_3$ (STO) is a representative perovskite oxide in a sense that it has many common structural features but exhibits a huge variety of physical phenomena/properties not only from itself but also by doping with defects or interfacing with other perovskite oxides. Various defects including intrinsic (e.g., oxygen vacancy[8−12]) and extrinsic (La,[13−15] Nb[16−19]) have been studied. Among them, self-doping by oxygen vacancies is of great importance because the oxygen vacancy has critical impacts on the wide spectrum of phenomena, such as the insulator-to-metal transition,[20,21] magnetoresistance,[21,22] superconductivity at

low temperatures,[23−25] magnetism,[26−29] and thermoelectricity.[30] Thus, STO is a good platform to investigate the phenomena relevant to oxygen vacancy in the perovskite oxide.

Once oxygen vacancy is introduced into STO, a primary concern is to find out the character of the doped electron by oxygen, which immediately affects the transport properties of the oxygen-deficient STO. Gong et al. reported that the carrier density of reduced STO increased linearly with the oxygen vacancy concentration.[12] That is, the oxygen vacancy was singly ionized. Because the two electrons are left behind upon creation of an oxygen vacancy, this behavior was explained in a two-band model where band electrons have very large effective mass in one of the two bands and the oxygen vacancies are implicitly assumed to be an isolated defect (Figure 1a). However, the carrier density tended to level off at a highly reduced state,[12] which could not be explained successfully by the singly ionized state. In our previous study by first-principles, we reported that the oxygen vacancies in highly reduced $SrTiO_{3−δ}$ tended to cluster in a linear way such as oxygen divacancies or linear clusters (Figure 1b), accompanied by electron localization.[31]

The oxygen vacancy clustering resulted in a flat band in a forbidden gap and consequently electron localization, which successfully explained the behavior of the carrier density in highly reduced STO. The photoluminescence found in reduced STO[32] could be also explained by defect states in a forbidden gap, while reorientation of pairs of vacancies[33] and inhomogeneous character[34] were suggested. Transmission electron
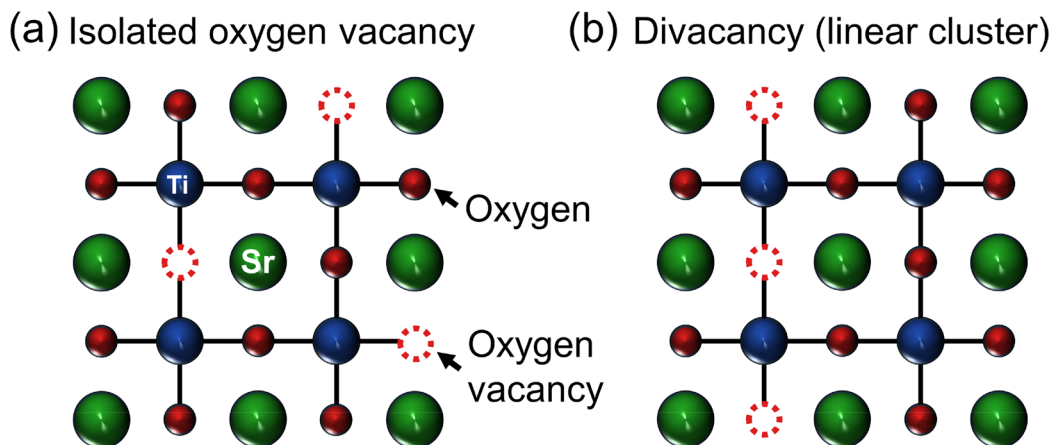
Figure 1. Schematic diagrams depicting the oxygen vacancy configurations of $SrTiO_{3-\delta}$ thin films in an (a) isolated state and (b) divacancy/linear cluster.

microscopy of $(SrTiO_3)_m/(SrTiO_{3-\delta})_n$ superlattices also showed the possibility of defect clustering.[35] Vacancy ordering was also reported in degraded $BaTiO_3$.[36] Thus, further experimental studies are needed to clarify the oxygen vacancy clustering in reduced STO. The previous first-principles study suggested that in the divacancy or linear cluster the electron localization occurs at the Ti ions located between oxygen vacancies, named an apical oxygen divacancy, leading to the change in electronic configuration from $3d^0$ to $3d^2$, with localized states in the band gap. Correspondingly, the valence state of the Ti ion is expected to change from +4 to +2. In this study, the carrier density behavior of the reduced STO thin films was studied with low-temperature postannealing, and the electronic state of the Ti ion was examined by photoemission spectroscopy to clarify the electronic state of the Ti ion. Further, diffuse X-ray scattering was used to verify the presence of the vacancy clusters and their crystallographic orientation. We report on the experimental verification of oxygen vacancy clustering and electron localization in perovskite STO.

STO thin films (100 nm thick) were deposited by pulsed laser deposition (PLD) on a $MgO(001)$ substrate at an ambient oxygen pressure in the range from 10^{-7} to 10^{-4} Torr while the substrate temperature was kept at 700 °C to obtain the oxygen deficiency. After deposition, all samples were fast cooled at the same deposition oxygen pressure to maintain the oxygen deficiency. When the ambient oxygen pressure became lower than 10^{-5} Torr, the STO films began to show a light gray color and simultaneously became conductive with large carrier densities, whereas STO films made at high ambient oxygen pressures became an insulator and transparent. Thus, the ambient oxygen pressure was kept at 10^{-7} Torr. First, the oxygen deficiency was examined by varying a cooling rate of the oxygen-deficient STO films. Equilibrium oxygen pressure during the cooling is far below the cooling oxygen pressure, causing the reduced STO films to be oxidized through oxygen vacancy migration during the cooling. This oxidation is well represented in the carrier density behavior with a cooling rate, shown in Figure S1. The faster the cooling rate, the higher the carrier density. The fast-cooled STO films had a carrier density of 6.7×10^{20} cm^{-3}. The high carrier densities in the reduced STO films ensured that the fast-cooled STO films contained a large concentration of oxygen vacancy.

Once highly reduced STO films were obtained, postannealing treatment was performed at an oxygen pressure of 10^{-2}

Torr and temperatures ranging from 200 to 550 °C, where the local rearrangement and/or migration of the oxygen vacancies are expected to occur during the annealing treatment. The local rearrangement could induce oxygen vacancy clustering without significant changes in the oxygen vacancy concentration, while migration could lead to oxygen exchange between the air and the film surface and a large change in the oxygen vacancy concentration. The freeze-in temperature (T_F)[37,38] was reported in oxide materials, where the oxygen exchange between the gas phase and oxides cannot occur readily below T_F. The oxygen vacancy (or cluster) migration will be greatly suppressed below T_F by the high activation energies (0.6−1.2 eV) in STO.[27,39] The postannealing temperature was intended to range from 200 to 550 °C to include the freeze-in temperature. The duration of the postannealing treatment was also varied from 20 to 60 min, and the resulting carrier density of the annealed STO films was measured with the annealing time.

Figure 2 shows the change in the carrier density of $SrTiO_{3-\delta}$ thin films with the postannealing temperature and time. The carrier density tended to decrease with increasing annealing
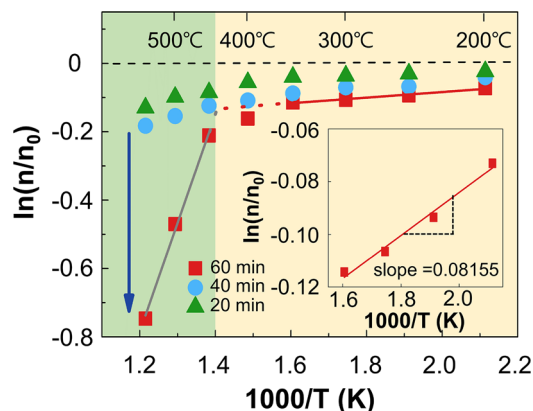
Figure 2. Carrier density of $SrTiO_{3-\delta}$ thin films with annealing temperature and time. The annealing process was performed by RTA at 10^{-2} Torr oxygen ambient pressure. Here, n_0 and n are the carrier density of $SrTiO_{3-\delta}$ thin films, as-deposited and postannealed, respectively. The binding energy of two oxygen vacancies in a divacancy form was estimated from the slope $(\delta\varepsilon/2k_B)$ of the plot in the inset, which is 0.35 eV.

temperature and time. The oxygen pressure (10^{-2} Torr) of the postannealing is much larger than the equilibrium oxygen pressure in the annealing temperature region. Therefore, the decrease in the carrier density is attributable to either the change in oxygen vacancy concentration or local rearrangement of the oxygen vacancy. Two different temperature regimes with a crossover temperature (T_{cr}) were found in the behavior of the carrier density with temperature. Below 440 °C, the carrier density decreased gradually with the annealing time and did not change further in annealing time longer than 60 min. Above 440 °C, the carrier density decreased rapidly with the annealing time, which is clearly seen at an annealing time of 60 min in Figure 2. Such high annealing temperatures above 440 °C allow easy oxygen vacancy migration, resulting in oxidation of the reduced STO films in an oxidizing environment and a correspondingly significant decrease in the carrier density. At annealing temperatures above 600 °C, the carrier density was too low to measure and became similar to that of stoichiometric STO films. It is noted that this T_{cr} (440 °C) is in a similar region as the freeze-in temperatures.[37,38] Electron paramagnetic resonance (EPR) study also showed that low-temperature annealing resulted in a small change in the oxygen vacancy concentration, while high-temperature annealing caused a significant change of the oxygen vacancy concentration, which could be attributed to the dependence of oxygen vacancy migration on temperature.[40]

Therefore, the postannealing at such low temperatures below 440 °C may not allow the long-range migration of oxygen vacancies, but the local rearrangement leading to vacancy clustering would be possible. The previous first-principles calculation on SrTiO$_{3-\delta}$ showed that the carrier density was in the range from $\delta/2$ to δ per unit volume, while the carrier density of a singly ionized and isolated oxygen vacancy is expected to be δ.[31] Then, a gradual decrease in carrier density with annealing time is understood in terms of the progressive clustering, accompanied by electron localization. Once the two different regimes were observed clearly in the carrier density behavior with the annealing temperature and time, the crossover temperature T_{cr} was also estimated using a divacancy model (see more detail in the Supporting Information). The model assumes that vacancies tend to cluster below T_{cr} due to the interaction between the vacancies, and the vacancies become an isolated form above T_{cr} due to the dominance of the thermal entropy effect. T_{cr} is compared with that obtained from the carrier density behavior shown in Figure 2.

In the model, the changes in the free energy ΔF_1 and ΔF_2 of the oxygen-deficient STO containing isolated oxygen vacancies and divacancies per unit cell, respectively, from the perfect crystal are expressed by the following relations

$$\Delta F_1 = (\delta m E_0 - k_B T \ln \Omega_1)/m$$
$$\Delta F_2 = [\delta m/2(2E_0 - \varepsilon) - k_B T \ln \Omega_2]/m \qquad (1)$$

where m is the number of unit cell in STO, δ is the concentration of the oxygen vacancy deficiency, ε is the interaction energy (or binding energy) of two oxygen vacancies in a divacancy form, E_0 is the internal energy of the isolated oxygen vacancy, and Ω is the number of configurations of the isolated oxygen vacancies or divacancies in the oxygen lattice sites of m unit cells. The interaction energy ε of 0.35 eV was obtained from extrapolation of the carrier density change at low temperatures (inset of Figure 2 and Supporting Information

section A). This is similar to the value obtained from the first-principles calculation.[31]

From the equilibrium condition ($\Delta F_1 = \Delta F_2$), the crossover temperature is expressed as a function of the oxygen deficiency δ by the following equation (see more detail in the Supporting Information):

$$T_{cr}(\delta) = \frac{\varepsilon}{k_B} \frac{\delta}{2} \left[3 \ln\left(\frac{3}{3-\delta}\right) + \delta \ln\left(\frac{3}{\delta} - 1\right) - \ln\left(\frac{2}{2-\delta}\right) \right.$$
$$\left. - \frac{\delta}{2} \ln\left(\frac{2}{\delta} - 1\right) \right]^{-1}$$

$$(2)$$

T_{cr} obtained at $\delta = 0.04$ is 437 °C, which is in good agreement with the crossover temperature (440 °C) obtained from the carrier density measurement, as shown in Figure 2. The value of $\delta = 0.04$ was extracted from fast-cooled films by Hall measurement. It is again worth mentioning that the crossover temperature is close to the freeze-in temperatures in perovskite oxides.[38] Therefore, contrary to the rapid decay of the carrier density of STO films annealed at high temperatures, the oxygen vacancy clustering successfully explains the gradual decrease in the carrier density of STO films annealed at low temperatures below T_{cr}.

Once oxygen vacancy clusters form, Ti ions located between the apical oxygen vacancies receive two electrons from each apical oxygen vacancies, resulting in the $3d^2$ electronic configuration of the Ti ion. Therefore, the electronic configuration of Ti is another important indication of the oxygen vacancy clustering, in addition to the carrier density behavior. The electronic configuration of Ti 3d in the oxygen-deficient STO films annealed at low temperatures (e.g., 250 °C, low enough to induce only local rearrangement of the oxygen vacancy and possibly clustering) was investigated by high-resolution photoemission spectroscopy (HR-PES) and was compared with fast-cooled STO films that are expected to exist primarily as an isolated form. Figure 3 shows Ti 3p spectra of the fast-cooled SrTiO$_{3-\delta}$ thin film before and after postannealing at a low temperature (250 °C, 60 min). The deconvolution of the spectra into Ti^{4+} (A), Ti^{3+} (B), and Ti^{2+} (C) clearly indicates that the intensity corresponding to the Ti^{2+} state (C) increases after the annealing. The Ti^{2+} valence state corresponds to a $3d^2$ electronic configuration. As described above, an electron is transferred from each apical oxygen vacancy to a Ti ion located between the apical oxygen divacancy and linear cluster. This leads to a localized state with an electronic configuration of Ti $3d^2$ because the Ti ion accepts two electrons from the oxygen vacancies, while the electronic configuration of Ti $3d^1$ (or Ti^{3+} valence state) exists in an isolated oxygen vacancy form. Therefore, the increase in the intensity of the Ti^{2+} valence state after low-temperature annealing is a consequence of the oxygen vacancy clustering in a linear way accompanied by strong electron localization at the Ti site.

PES spectra covering a wide range of binding energies including a gap state as well as Ti 3p, Sr 4p, and the O 2p-derived valence band, are also shown in Figure S3. The valence band maximum consists of mostly O 2p, which is well recognized as a common feature in transition metal oxides. Compared with stoichiometric STO, an additional peak appears above the valence band (or within a forbidden band) in the SrTiO$_{3-\delta}$ thin films in both the as-deposited and annealed states. The additional peak is attributed to a localized state in
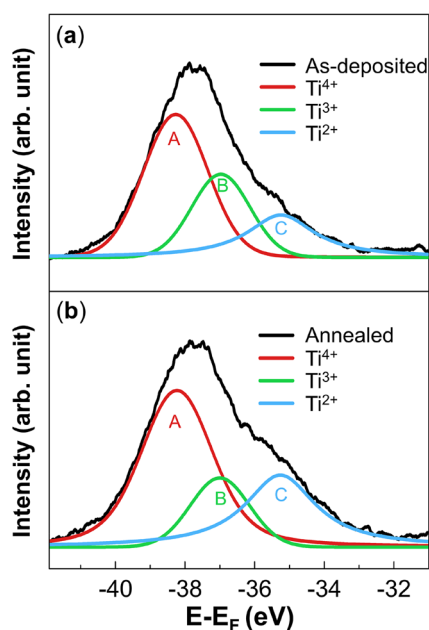
Figure 3. PES spectra of Ti 3p for fast-cooled $SrTiO_{3-\delta}$ thin films (a) before and (b) after postannealing at a low temperature (250 °C, 60 min.). A, B, and C peaks after deconvolution of the spectra correspond to Ti^{4+}, Ti^{3+}, and Ti^{2+}, respectively.

the forbidden band accompanied by the formation of the Ti^{3+} state. It has also been reported in oxygen-deficient $SrTiO_{3-\delta}$,[41,42] as well as other reduced transition metal oxides such as $TiO_{2-\delta}$,[43] $CaVO_{3-\delta}$, and $SrVO_{3-\delta}$,[44] which have $3d^1$ electronic configurations (i.e., Ti^{3+} and V^{3+} valence states). Although the highly reduced STO films were fast-cooled in the deposition chamber after deposition, the cooling was not fast at low temperatures due to low thermal conductions at low cooling pressures. The fast-cooled STO films are very likely to have some amount of oxygen vacancy clusters, which is supported by the PES result before annealing showing the Ti^{2+} valence state in the fast-cooled STO films.

To examine the presence and aligned direction of oxygen vacancy clustering, we also performed diffuse X-ray scattering to look for further structural evidence. Figure 4 shows reciprocal space maps around the (−101) Bragg reflection for postannealed films at 350 °C. The distinct line shape patterns horizontally extending across both H and K directions near the Bragg peak suggest a 2D planar feature in the reciprocal space volume, which can be attributed to the linear clustering of oxygen vacancies along the crystallographic [001] direction in
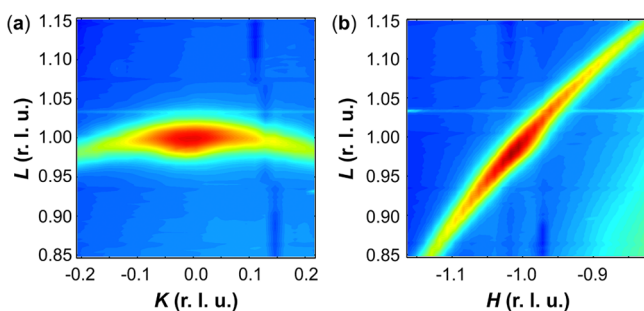
Figure 4. X-ray diffuse scattering (a) 2D K−L and (b) H−L views around the (−101) Bragg peak of postannealed a $SrTiO_{3-\delta}$ thin film at 350 °C.

real space. In contrast, the as-grown films do not show the linear feature (Figure S4).

In conclusion, we experimentally verified oxygen vacancy clustering and ensuing electron localization in highly reduced $SrTiO_{3-\delta}$ thin films by carrier density measurement, photoemission spectroscopy, and diffuse X-ray scattering. When the highly reduced $SrTiO_{3-\delta}$ thin films were postannealed at temperatures (below 440 °C) sufficiently low to allow local realignment of oxygen vacancies but not their long-range migration, the carrier density of the $SrTiO_{3-\delta}$ thin films was gradually reduced by annealing treatment. This transport behavior results from electron localization through the oxygen vacancy clustering in a linear way. Photoemission spectroscopy study shows that the Ti^{2+} valence state of the highly reduced $SrTiO_{3-\delta}$ thin films increases after low-temperature annealing, verifying the oxygen vacancy clustering in a linear manner. Diffuse X-ray scattering analysis also indicates the presence of the linear clusters and further reveals the orientation of the linear clusters along the specific geometric [001] direction in a perovskite oxide. This study demonstrates experimental evidence of the oxygen vacancy clustering in STO. This result can be extended to a wide variety of perovskite oxides because STO is an archetypal perovskite oxide in terms of their physical phenomena and properties. Therefore, this study will provide a new aspect in understanding oxides with defects.

■ EXPERIMENTAL METHODS

Sample Preparation. We used the PLD technique (KrF excimer laser, λ = 248 nm) to synthesize all $SrTiO_{3-\delta}$ samples studied in this work. The substrate used for film deposition is 5 × 5 mm^2 MgO(001). The stoichiometric STO target was used while an ambient oxygen pressure of 10^{-7} Torr was used to induce oxygen deficiency in STO thin films. The film thickness was kept at 100 nm, which was estimated from reflection high-energy electron diffraction (RHEED) oscillations.

Transport Characterization. The Hall measurement was carried out by the four-probe dc technique in the Van der Pauw geometry. The carrier density was determined by $n = 1/(t \cdot e \cdot R_H)$, where t is the thickness of the film and R_H is the measured 2D Hall coefficient. For the Hall measurements, the magnetic field H was varied between ±0.55 T.

Photoemission Spectroscopy. HR-PES at the Pohang Light Source (PAL, 8A2 HR-PES beamline equipped with an electron analyzer (SES100, Gamma-Data Scienta)) was used for this experiment. The measurement was performed in an ultrahigh vacuum (UHV) chamber with a base pressure of 5×10^{-10} Torr. The binding energies of the spectra and Fermi level were calibrated with respect to the binding energy of the Au foil. The PES spectra are sensitive to surface morphology and contamination, which requires sputtering to clean a sample surface of contamination followed by annealing to make the sample surface smooth from roughening of the sample surface. However, in our study, the sputtering alone was carried out to clean the sample surface in a condition not to induce nonstoichiometry at the sample surface because annealing can influence the electronic state of the sample, that is, Ti valence states. Despite the sputtering not being followed by annealing, sample surfaces were kept smooth within the rms roughness of 0.4 nm after the sputtering (see more detail in the Supporting Information).

X-ray Diffuse Scattering Characterization. X-ray diffuse scattering measurements were performed on a five-circle diffractometer with χ-circle geometry using an X-ray energy

of 20 keV (wavelength $\lambda = 0.6197$ Å) at sector 12-ID-D of the Advanced Photon Source (APS), Argonne National Laboratory. The X-ray beam at beamline 12-ID-D had a total flux of 4.0×10^{12} photons/s and was vertically focused by a beryllium compound refractive lens to a beam profile below 100 μm. The weak diffuse scattering signal was obtained by collecting a 3D reciprocal space map (3DRSM) around a primary Bragg peak of a $SrTiO_{3-\delta}$ thin film using a sequence of two-dimensional images acquired with a pixel 2D array area detector (Dectris PILATUS-1 mm Si 100 K). The overall 3DRSMs were deduced and constructed by the APS open access software rsMap3D.

■ ASSOCIATED CONTENT

ⓢ Supporting Information

The Supporting Information is available free of charge on the ACS Publications website at DOI: 10.1021/acs.jpclett.7b01348.

> Carrier density behavior of the $SrTiO_{3-\delta}$ thin films with various cooling rates (Figure S1), detailed derivation of the crossover temperature, AFM images of STO film surfaces after measuring the PES (Figure S2), surface treatment of the film surface prior to PES measurement, PES spectra of fast-cooled and annealed $SrTiO_{3-\delta}$ thin films at 250 °C/60 min. (Figure S3) showing a wide range of a binding energies including a gap state as well as Ti 3p, Sr 4p, and O 2p-derived valence bands, and X-ray diffuse scattering around the (−101) Bragg peak of an as-grown $SrTiO_{3-\delta}$ thin film (Figure S4) (PDF)

■ AUTHOR INFORMATION

Corresponding Author
*E-mail: jclee@skku.edu.

ORCID ⓘ

Jaichan Lee: 0000-0002-2730-9492

Notes

The authors declare no competing financial interest.

■ ACKNOWLEDGMENTS

■ REFERENCES

(1) Bednorz, J. G.; Muller, K. A. Possible High T_c Superconductivity in the Ba-La-Cu-O System. *Z. Phys. B: Condens. Matter* **1986**, *64*, 189−193.

(2) Maeda, H.; Tanaka, Y.; Fukutomi, M.; Asano, T. A New High-T_c Oxide Superconductor without a Rare Earth Element. *Jpn. J. Appl. Phys.* **1988**, *27*, L209−L210.

(3) Guo, Z. B.; Du, Y. W.; Zhu, J. S.; Huang, H.; Ding, W. P.; Feng, D. Large Magnetic Entropy Change in Perovskite-Type Manganese. *Phys. Rev. Lett.* **1997**, *78*, 1142−1145.

(4) Eerenstein, W.; Mathur, N. D.; Scott, J. F. Multiferroic and Magnetoelectric Materials. *Nature* **2006**, *442*, 759−765.

(5) Imada, M.; Fujimori, A.; Tokura, Y. Metal-Insulator Transitions. *Rev. Mod. Phys.* **1998**, *70*, 1039−1263.

(6) Homes, C. C.; Vogt, T.; Shapiro, S. M.; Wakimoto, S.; Ramirez, A. P. Optical Response of High-Dielectric-Constant Perovskite-Related Oxide. *Science* **2001**, *293*, 673−676.

(7) Lee, D.; Lu, H.; Choi, S.-Y.; Li, S.-D.; Ryu, S.; Paudel, T. R.; Song, K.; Mikheev, E.; Lee, S.; Stemmer, S.; et al. Emergence of Room-Temperature Ferroelectricity at Reduced Dimensions. *Science* **2015**, *349*, 1314−1317.

(8) Lee, C.; Destry, J.; Brebner, J. L. Optical Absorption and Transport in Semiconducting $SrTiO_3$. *Phys. Rev. B* **1975**, *11*, 2299−2310.

(9) Crandles, D. A.; Nicholas, B.; Dreher, C.; Homes, C. C.; McConnell, A. W.; Clayman, B. P.; Gong, W. H.; Greedan, J. E. Optical Properties of Highly Reduced $SrTiO_{3-x}$. *Phys. Rev. B: Condens. Matter Mater. Phys.* **1999**, *59*, 12842−12846.

(10) Kalabukhov, A.; Gunnarsson, R.; Borjesson, J.; Olsson, E.; Claeson, T.; Winkler, D. Effect of Oxygen Vacancies in the $SrTiO_3$ Substrate on the Electrical Properties of the $LaAlO_3/SrTiO_3$ Interface. *Phys. Rev. B: Condens. Matter Mater. Phys.* **2007**, *75*, 121404.

(11) Siemons, W.; Koster, G.; Yamamoto, H.; Harrison, W. A.; Lucovsky, G.; Geballe, T. H.; Blank, D. H. A.; Beasley, M. R. Origin of Charge Density at $LaAlO_3$ on $SrTiO_3$ Heterointerfaces: Possibility of Intrinsic Doping. *Phys. Rev. Lett.* **2007**, *98*, 196802.

(12) Gong, W.; Yun, H.; Ning, Y. B.; Greedan, J. E.; Datars, W. R.; Stager, C. V. J. Oxygen-Deficient $SrTiO_{3-x}$, $x = 0.28$, 0.17, and 0.08. Crystal Growth, Crystal Structure, Magnetic, and Transport Properties. *J. Solid State Chem.* **1991**, *90*, 320−330.

(13) Son, J.; Moetakef, P.; Jalan, B.; Bierwagen, O.; Wright, N. J.; Engel-Herbert, R.; Stemmer, S. Epitaxial $SrTiO_3$ Films with Electron Mobilities Exceeding 30,000 $cm^2V^{-1}s^{-1}$. *Nat. Mater.* **2010**, *9*, 482−484.

(14) Tang, C. Q.; Xia, Z.; Yao, S.; Chen, S. Dependence of the Electric Properties and the Positron Lifetimes on the Dopant Content in La-doped $SrTiO_3$. *Cryst. Res. Technol.* **1996**, *31*, 821−826.

(15) Ohta, S.; Nomura, T.; Ohta, H.; Koumoto, K. High-Temperature Carrier Transport and Thermoelectric Properties of Heavily La- or Nb- doped $SrTiO_3$ Single Crystals. *J. Appl. Phys.* **2005**, *97*, 034106.

(16) Tufte, O. N.; Chapman, P. W. Electron Mobility in Semiconducting Strontium Titanate. *Phys. Rev.* **1967**, *155*, 796−802.

(17) Tufte, O. N.; Stelzer, E. L. Magnetoresistance in Semiconducting Strontium Titanate. *Phys. Rev.* **1968**, *173*, 775−777.

(18) Ohta, S.; Nomura, T.; Ohta, H.; Hirano, M.; Hosono, H.; Koumoto, K. Large Thermoelectric Performance of Heavily Nb-Doped $SrTiO_3$ Epitaxial Film at High Temperature. *Appl. Phys. Lett.* **2005**, *87*, 092108.

(19) Gregory, B.; Arthur, J.; Seidel, G. Measurements of the Fermi Surface of $SrTiO_3$:Nb. *Phys. Rev. B: Condens. Matter Mater. Phys.* **1979**, *19*, 1039−1048.

(20) Calvani, P.; Capizzi, M.; Donato, F.; Lupi, S.; Maselli, P.; Peschiaroli, D. Observation of a Midinfrared Band in $SrTiO_{3-y}$. *Phys. Rev. B: Condens. Matter Mater. Phys.* **1993**, *47*, 8917−8922.

(21) Liu, Z. Q.; Leusink, D. P.; Wang, X.; Lu, W. M.; Gopinadhan, K.; Annadi, A.; Zhao, Y. L.; Huang, X. H.; Zeng, S. W.; Huang, Z.; et al. Metal-Insulator Transition in $SrTiO_{3-x}$ Thin Films Induced by Frozen-Out Carriers. *Phys. Rev. Lett.* **2011**, *107*, 146802.

(22) Frederikse, H. P. R.; Hosler, W. R.; Thurber, W. R. Magnetoresistance of Semiconducting $SrTiO_3$. *Phys. Rev.* **1966**, *143*, 648−651.

(23) Appel, J. Soft-Mode Superconductivity in $SrTiO_{3-x}$. *Phys. Rev.* **1969**, *180*, 508−516.

(24) Binnig, G.; Hoenig, H. E. Energy Gap of the Superconducting Semiconductor $SrTiO_{3-x}$ Determined by Tunneling. *Solid State Commun.* **1974**, *14*, 597−601.

(25) Schooley, J. F.; Hosler, W. R.; Cohen, M. L. Superconductivity in Semiconducting $SrTiO_3$. *Phys. Rev. Lett.* **1964**, *12*, 474−475.

(26) Rice, W. D.; Ambwani, P.; Bombeck, M.; Thompson, J. D.; Haugstad, G.; Leighton, C.; Crooker, S. A. Persistent Optically Induced Magnetism in Oxygen-Deficient Strontium Titanate. *Nat. Mater.* **2014**, *13*, 481−487.

(27) Hou, Z. F.; Terakura, K. Defect States Induced by Oxygen Vacancies in Cubic $SrTiO_3$: First-Principles Calculations. *J. Phys. Soc. Jpn.* **2010**, *79*, 114704.

(28) Pavlenko, N.; Kopp, T.; Tsymbal, E. Y.; Mannhart, J.; Sawatzky, G. A. Oxygen Vacancies at Titanate Interfaces: Two-Dimensional Magnetism and Orbital Reconstruction. *Phys. Rev. B: Condens. Matter Mater. Phys.* **2012**, *86*, 064431.

(29) Lin, C. W.; Demkov, A. A. Electron Correlation in Oxygen Vacancy in $SrTiO_3$. *Phys. Rev. Lett.* **2013**, *111*, 217601.

(30) Srivastava, D.; Norman, C.; Azough, F.; Schafer, M. C.; Guilmeau, E.; Kepaptsoglou, D.; Ramasse, Q. M.; Nicotra, G.; Freer, R. Tuning the Thermoelectric Properties of A-Site Deficient $SrTiO_3$ Ceramics by Vacancies and Carrier Concentration. *Phys. Chem. Chem. Phys.* **2016**, *18*, 26475−26486.

(31) Cuong, D. D.; Lee, B.; Choi, K. M.; Ahn, H. S.; Han, S.; Lee, J. Oxygen Vacancy Clustering and Electron Localization in Oxygen-Deficient $SrTiO_3$: LDA + U Study. *Phys. Rev. Lett.* **2007**, *98*, 115503.

(32) Kan, D. S.; Terashima, T.; Kanda, R.; Masuno, A.; Tanaka, K.; Chu, S. C.; Kan, H.; Ishizumi, A.; Kanemitsu, Y.; Shimakawa, Y.; et al. Blue-Light Emission at Room Temperature from Ar^+-Irradiated $SrTiO_3$. *Nat. Mater.* **2005**, *4*, 816−819.

(33) Cordero, F. Hopping and Clustering of Oxygen Vacancies in $SrTiO_3$ by Anelastic Relaxation. *Phys. Rev. B: Condens. Matter Mater. Phys.* **2007**, *76*, 172106.

(34) Szot, K.; Speier, W.; Carius, R.; Zastrow, U.; Beyer, W. Localized Metallic Conductivity and Self-Healing during Thermal Reduction of $SrTiO_3$. *Phys. Rev. Lett.* **2002**, *88*, 075508.

(35) Muller, D. A.; Nakagawa, N.; Ohtomo, A.; Grazul, J. L.; Hwang, H. Y. Atomic-Scale Imaging of Nanoengineered Oxygen Vacancy Profiles in $SrTiO_3$. *Nature* **2004**, *430*, 657−661.

(36) Woodward, D. I.; Reaney, I. M.; Yang, G. Y.; Dickey, E. C.; Randall, C. A. Vacancy Ordering in Reduced Barium Titanate. *Appl. Phys. Lett.* **2004**, *84*, 4650−4652.

(37) Sasaki, K.; Maier, J. Low-Temperature Defect Chemistry of Oxides. I. General Aspects and Numerical Calculations. *J. Appl. Phys.* **1999**, *86*, 5422−5433.

(38) Claus, J.; Leonhardt, M.; Maier, J. Tracer Diffusion and Chemical Diffusion of Oxygen in Acceptor Doped $SrTiO_3$. *J. Phys. Chem. Solids* **2000**, *61*, 1199−1207.

(39) Wagner, S. F.; Warnke, C.; Menesklou, W.; Argirusis, C.; Damjanovic, T.; Borchardt, G.; Ivers-Tiffee, E. Enhancement of Oxygen Surface Kinetics of $SrTiO_3$ by Alkaline Earth Metal Oxides. *Solid State Ionics* **2006**, *177*, 1607−1612.

(40) Zvanut, M. E.; Jeddy, S.; Towett, E.; Janowski, G. M.; Brooks, C.; Schlom, D. An Annealing Study of an Oxygen Vacancy Related Defect in $SrTiO_3$ Substrate. *J. Appl. Phys.* **2008**, *104*, 064122.

(41) Dudy, L.; Sing, M.; Scheiderer, P.; Denlinger, J. D.; Schutz, P.; Gabel, J.; Buchwald, M.; Schlueter, C.; Lee, T. L.; Claessen, R. In Situ Control of Separate Electronic Phases on $SrTiO_3$ Surfaces by Oxygen Dosing. *Adv. Mater.* **2016**, *28*, 7443−7449.

(42) Wunderlich, W.; Ohta, H.; Koumoto, K. Enhanced Effective Mass in Doped $SrTiO_3$ and Related Perovskites. *Phys. B* **2009**, *404*, 2202−2212.

(43) Tait, R. H.; Kasowski, R. V. Ultraviolet Photoemission and Low-Energy-Electron Diffraction Studies of TiO_2 (Rutile) (001) and (110) Surfaces. *Phys. Rev. B: Condens. Matter Mater. Phys.* **1979**, *20*, 5178−5191.

(44) Aiura, Y.; Iga, F.; Nishihara, Y.; Ohnuki, H.; Kato, H. Effect of Oxygen Vacancies on Electronic States of $CaVO_{3−\delta}$ and $SrVO_{3−\delta}$: A Photoemission Study. *Phys. Rev. B: Condens. Matter Mater. Phys.* **1993**, *47*, 6732−6734.